# SINGLE CRYSTAL SUPERALLOYS:

# THE TRANSITION FROM PRIMARY TO SECONDARY CREEP

G.L. Drew, R.C. Reed\*, K. Kakehi\*\*, and C.M.F. Rae

University of Cambridge, Rolls-Royce University Technology Partnership, Department of Materials Science and Metallurgy, Pembroke Street, Cambridge, CB2 3QZ.

\*University of British Columbia, 309-6350 Stores Road, Vancouver V6T 1Z4

\*\*Department of Mechanical Engineering, Tokyo Metropolitan University, Minami Osawa 1-1, Hachioji TOKYO, 192-0397 Japan

Superalloys, Creep, Activation Energy,

#### Abstract

In this paper we compare the effect of stress, orientation and alloy composition on primary and secondary creep rate in a number of single crystal alloys. The activation energies and stress dependence of primary and secondary creep, measured in the alloy CMSX-4, show a distinctive low activation energy associated with stacking fault shear during primary creep which disappears at low stress. Twostage creep tests show that a fully developed dislocation network, introduced into the microstructure by limited deformation at 950°C, results in a substantial drop in primary creep strain during subsequent testing at 750°C. Comparison with identically-oriented samples without prestrain confirms the role of dislocation networks in the  $\gamma$ channels as the major hardening mechanism and shows that secondary creep is unaffected by the pre-strain. These observations are inconsistent with existing understanding of the transition between primary and secondary creep in some important respects. We argue that the mechanisms producing primary and secondary creep strain are similar, but that the secondary creep rate is determined by the rate of formation of defects at the  $\gamma/\gamma'$  interface. This enables many aspects of the dependence of creep rate on orientation, alloy composition and micro-structure to be rationalised.

## Introduction

In cooled single crystal turbine blades the majority of the load [1] is borne by the colder webs of the blade operating at temperatures calculated to be as low as 700°C. Thus, although much emphasis has been put on the development of superb high temperature properties for these materials, the performance of the blade as a whole depends critically on the low temperature properties. Work over many years has shown that the creep behaviour at low temperatures (750°C-850°C) is extraordinarily sensitive to changes in orientation, composition and the heat-treated microstructure [2,3,4,5,6,7,8], yet the mechanistic origins of these effects

are not fully established. In this paper we are able to rationalise some of these effects by focusing on the nature of the processes occurring during primary and secondary creep, and in the transition period between the two.

In the temperature range 750°C to 850°C, creep behaviour is dominated by rapid initial primary creep following an incubation period, provided that a threshold stress is exceeded. Both processes are a sensitive function of the applied stress and the sample orientation, [2,4,9]. The primary creep can be as high as 10-15% in a constant load test at orientations some degrees away from the <001> orientation, and dominates the behaviour throughout the life: tests which exhibit a high primary creep have high secondary creep rates and short rupture lives [2,4]. It is not clear to what extent this is due to an intrinsic link between the mechanisms of primary and secondary creep mechanisms, or the increase in stress caused by the reduction in cross section. The extent of primary creep and the sensitivity to orientation is also a strong function of the alloy composition, with cobalt and rhenium in particular promoting high primary creep [8,10] and tantalum reducing it. The differences in composition between such alloys are often slight and merit further investigation in order to incorporate this 'orientation resilience' into new alloys thus allowing for greater angular tolerances during casting and production and thus higher yields.

### Primary creep:

There is a general consensus [2,4,5] that the dominant mechanism during primary creep is shear of the  $\gamma$  and  $\gamma'$  by dislocations separated by intrinsic and extrinsic stacking faults (and a narrow anti-phase boundary fault in the  $\gamma'$  [11]) combining to give an overall Burgers vector a<112>. The ribbons are able to cut through the  $\gamma$  and  $\gamma'$  phases without leaving dislocation debris at the interface. Stacking fault shear was confirmed as the major cause of the deformation strain by examining the rotation of the tensile axis and the anisotropy of the cross section, both of which are clearly characteristic of <112>{111} slip. The extent of

the primary creep correlates well with the activation of secondary slip systems, the best creep performance coming from orientations near [001], where four slip systems are equally stressed, and along the [001]-[011] symmetry boundary where two systems are equally favoured. The rotation necessary for the tensile axis to reach a slip symmetry boundary, a, was considered to be the prime determinant of the creep performance, [2]. Later studies [4] demonstrated that the extent of primary creep can be rationalised by this parameter, α, alone. However, microstructural evidence [12] reveals that the hardening process is more complex than this. Even for specimens oriented for single slip, conjugate slip systems operate from an early stage and the transition to secondary creep occurs long before the tensile axis rotates to the symmetry boundary. Thus the significance of the proximity of the symmetry boundary is the relative activity on these systems (and possibly others in the  $\gamma$  matrix) throughout primary creep, and thus the frequency of interactions leading to hardening.

In a previous paper [9] we presented a framework for the mechanisms controlling the deformation behaviour at low temperatures. High strain rates in primary creep require the rapid nucleation and propagation of a<112>{111} dislocations and are reduced by work-hardening from both stacking fault ribbons and dislocations in the y. This produces a pattern of orientation dependence similar to that established by MacKay [2], but, by explaining some of the micro-structural inconsistencies, satisfies recent results more accurately [9,13]: in particular the very low creep rates observed around the <012> pole. The basic pattern of orientation dependence is maintained over a wide range of alloy compositions, but the contribution of each of the components - nucleation, propagation and work-hardening - varies. This leads to immensely complex behaviour, for example: the  $\gamma/\gamma'$  misfit and  $\gamma'$  volume fraction affects the propagation of dislocations in the y leading to accelerated or reduced work-hardening, Using this approach it is possible to rationalise the reversal in the orientation dependence of the [111] and [001] tensile axes through the effect of heat treatment in changing the  $\gamma'$  volume fraction [3]. Cobalt and rhenium content affect superlattice stacking fault propagation through the two-phase structure, explaining the observation that some alloys appear to be unusually sensitive to the effects of orientation; others are very tolerant showing little primary creep over a wide range of orientations [8].

# Secondary creep:

Unlike primary creep there is no consensus over the nature of the predominant deformation mechanism of secondary creep. Long ago Leverant and Kear and Oblak [14] measured the activation energies for primary and secondary creep in the alloy MarM200 as 275 kJmol<sup>-1</sup> and 627 kJmol<sup>-1</sup> respectively, and thus proposed that a different mechanism takes over at the start of secondary or steady state creep.

They argued that the rate controlling mechanism in primary creep is vacancy diffusion related glide. As fine dislocation networks develop to produce secondary creep, interstitial defects become more numerous through dislocation cutting and become the rate controlling diffusion process. Alternatively, Sass, Glatzel and Feller-Kneipmeier [15] conclude, on the basis of micro-structural observations, that stacking fault shear accounts for primary creep and <110> {111} shear in the  $\gamma$  and increasingly of the  $\gamma$ ' as APB pairs accounts for the secondary creep. This is inconsistent with the rotation of the tensile axis and the shear [4].

## **Experimental**

## Creep tests:

Uniaxial creep tests were performed under constant load at the conditions listed in Table 1. When the tests were interrupted the stress was slightly reduced before cooling to below 400°C, then the specimen unloaded, cooled and removed.

The two-stage creep tests were performed on pairs of specimens cut from the same bar, thus having the same orientation. The stress and temperature at which the prestrain was performed (detailed in Table 1) were chosen to produce a network of dislocations confined to the  $\gamma$ , but avoiding the early stages of rafting. Following the prestrain, the specimens were cooled under reduced load at  $0.17^{\circ}\text{Cs}^{-1}$ , soaked at  $750^{\circ}\text{C}$  for 0.5-1 hour and reloaded to 750MPa taking into account the reduction in cross-sectional area caused by the pre-strain.

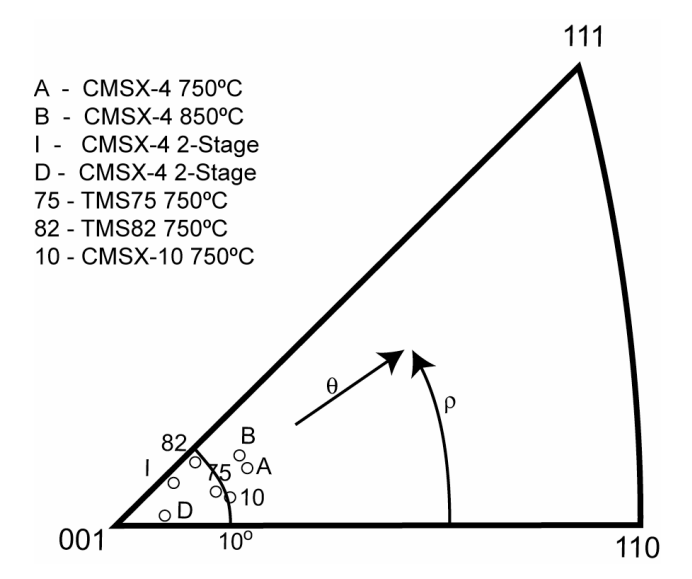


Figure 1. Orientations of the tensile axes for creep tests (Table 1 gives  $\theta$  and  $\rho$  values).

Two sets of specimens were cut from two single slabs of CMSX-4, having very similar orientations, A and B, shown in Figure 1. One set was tested at 750°C and the other at 850°C, each set under a range of stresses between 750 MPa

and 450 MPa. One further test was arrested at the beginning of secondary creep at 750°C and 750MPa. For each orientation the activation energy for secondary creep and the stress dependence was determined. Secondary creep was established isothermally at 750°C and 850°C, after which the temperature was dropped in 20° increments and the strain rate, §, measured, before returning to the original temperature. For the 750°C test, § was measured between 710°C and 770°C and for the 850°C test & was measured between 790°C to 850°C. Following this temperature excursion the stress was reduced and again § measured. Separate tests were required to assess the activation energy for primary creep as the high strain rate lasts only a few hours and does not achieve a constant rate. Activation energies were estimated by comparing the primary creep rates at 750°C and 850°C from the orientations A and B since these orientations were very close, to each other. Full details of these tests are summarised in Table 1.

Following the tests, the eccentricity of the samples at 750°C and 750 MPa were measured to characterise the slip systems operating. Measurements were made at Rolls-Royce Ltd using a Leitz co-ordinate measurement system. The radius of the gauge length was measured every 5° and at 2mm intervals along the gauge length. Results from orientation A interrupted at the beginning of secondary creep are compared with the failed sample of the same orientation.

## Table 1. Details of creep tests reported in this paper.

# Other Alloys:

Creep tests at 750°C and at the stresses 650MPa and 750MPa were performed on the alloys CMSX-10, TMS 75 and TMS 82, For each alloy two or three specimens of identical orientations were used, Figure 1. Comparison of the secondary creep rates allows the stress dependence of the secondary creep rates to be measured.

# Microstructural examination

Samples were sectioned either perpendicular to the tensile axis or along the primary slip plane as identified by a back-reflection Laue X-Ray. Discs were thinned mechanically and polished by a twin jet polisher using a solution of 10% perchloric acid in methanol at -5°C and 22 V. Foils were examined in a JEOL 2000FX transmission electron microscope

#### Results

## Activation energies and strain dependence:

Stress strain curves of the creep tests used for the calculation of activation energies and stress dependence of the alloy CMSX-4 at 850°C, and several alloys at 750°C are shown in Figures 2 and 3.

Activation energies for primary and secondary creep were calculated from the gradient of an Arhenius plot, Figure 4, and are summarised in Table 2. The creep rate was established at  $750^{\circ}$ C and re-measured at  $750^{\circ}$ C after the temperature excursion. In both cases the strain rate at the second period of creep is slightly higher, introducing an error of  $\pm$  15 kJmol<sup>-1</sup> at  $850^{\circ}$ C and  $\pm$  5 kJmol<sup>-1</sup> at  $750^{\circ}$ C.

Specimen	Orientation	Temp °C	Stress	Ámay	Ámin	Life	Final	Primary
	ρ/θ	Temp c	MPa	ð <sub>max</sub> s <sup>-1</sup>	ð <sub>min</sub> S <sup>-1</sup>	h	Strain%	Strain%
A	12.7 / 24.4	750°C	750	4.4E-6	8.0E-8	410h	23.3	6.3
CMSX-4					1.3E-6	8h <sup>1</sup>	8.6	
	12.7 / 24.4	750°C	650	6.0E-7	2.8E-9	2804 <sup>1</sup>	7.9	4.3
	12.7 / 24.4	750°C	550	4.4E-9	-	665 <sup>1</sup>	0.73	0.8
В	12.9 / 31.3	850°C	750	5.0E-5	2.6E-6	10	20.3	2.9
	12.9 / 31.3	850°C	650	1.3E-5	2.7E-7	82	20.5	2.0
	12.9 / 31.3	850°C	550	1.3E-6	2.8E-8	517	17.68	0.5
D	3.7/12.2	750°C	750	1.3E-6	8.6E-9	1824h	13.5	4.5
D*	3.7/12.2	950°C/750°C	485/750	6.1E-8	7.8E-9	2080h	16	2.0
I	6.1/43.3	750°C	750	2.8E-6	-	13.5h <sup>1</sup>	1	-
I*	6.1/43.3	950°C/750°C	485/750	3.3E-7	-	2.8 h <sup>1</sup>	0.4	-
TMS75	9/18	750°C	750	2.7E-5	2.2E-6	17.2	36	22.5
TMS82	8.5/37	750°C	750	1.6E-6	3.3E-8	427 <sup>1</sup>	11	4
CMSX-10	10.5/13	750°C	750	2.6E-6	4.4E-8	411	22.4	6.5

<sup>\*</sup>Two stage tests, <sup>1</sup>Tests interrupted before failure.

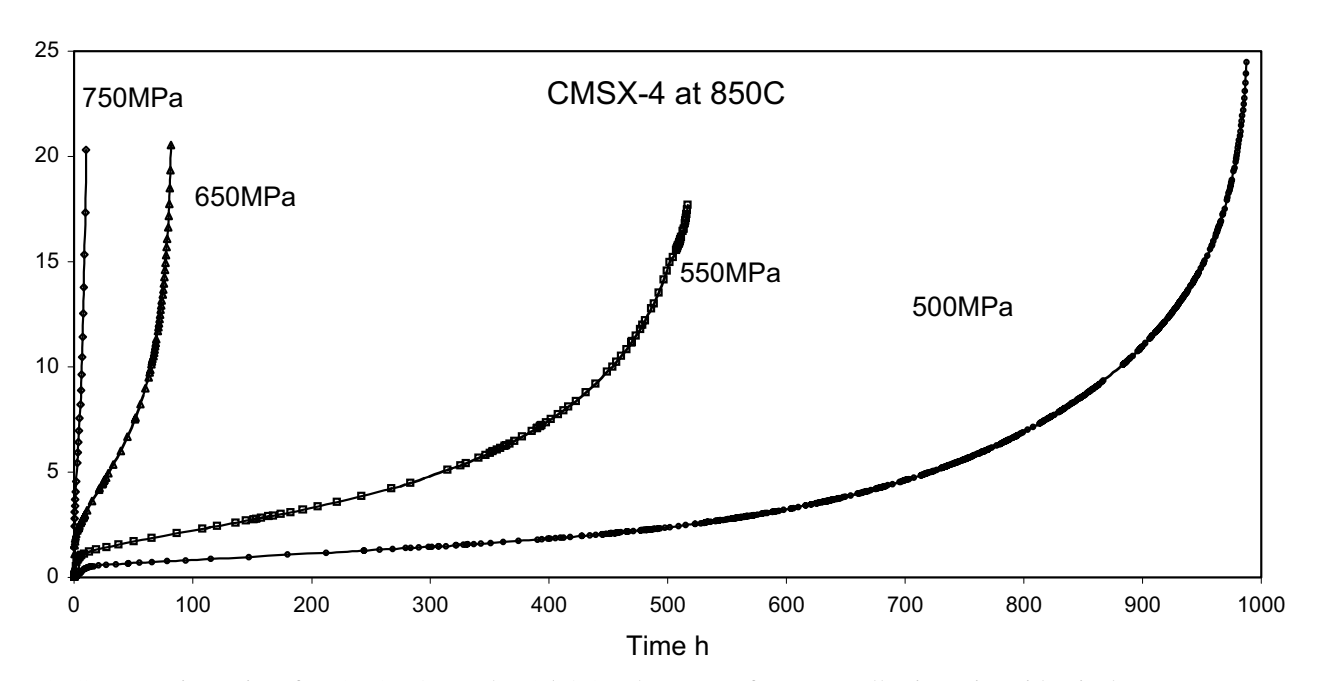


Figure 2 Creep strain vs time for CMSX-4 tested at 850°C and a range of stresses (all orientations identical).

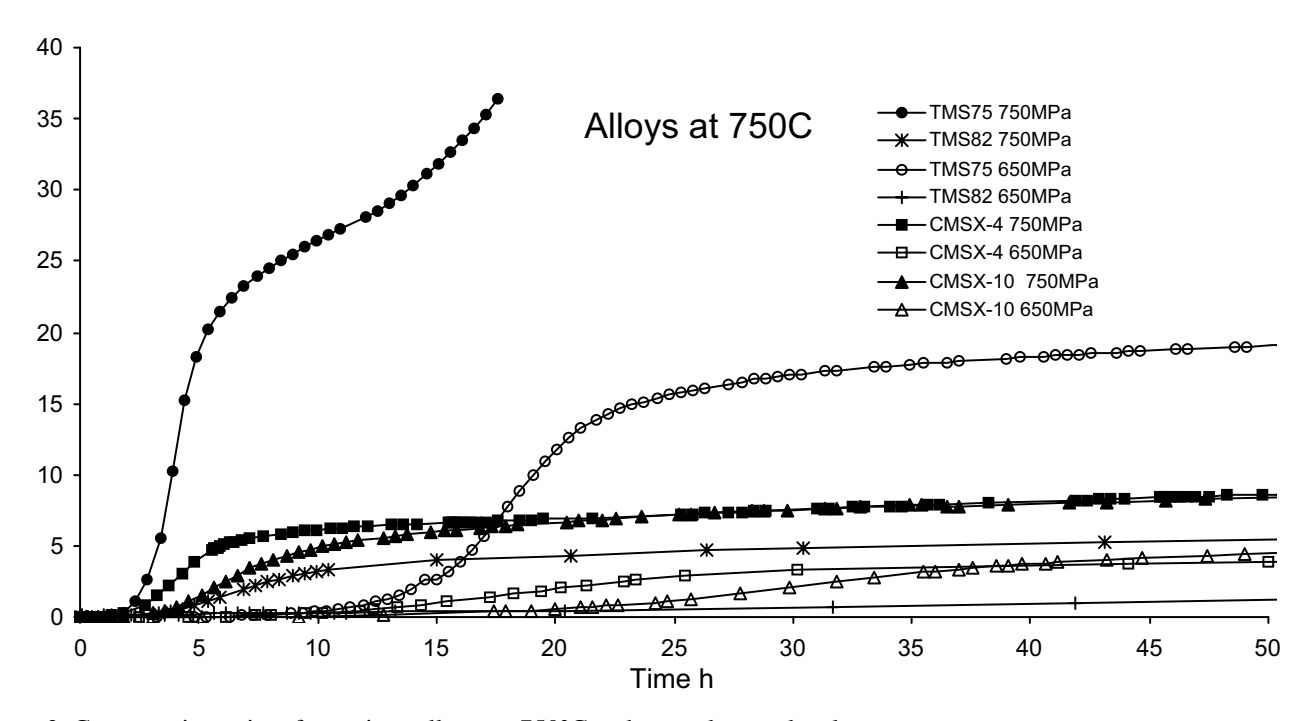


Figure 3 Creep strain vs time for various alloys at 750°C and several stress levels.

Comparison was made between activation energies obtained for secondary creep from the temperature drop tests and from two separate tests. A and B. The latter gives a value of  $505 \text{ kJmol}^{-1}$ , in good agreement when the creep rates from the separate tests were moderated to take account of the higher primary creep strain, and therefore stress, at  $750^{\circ}$ C. Creep rates were reduced by the factor  $\epsilon^{10}$  where  $\epsilon$  is the strain at the evaluation point. This was not necessary for the temperature drop test or for primary creep

activation energies given in Table 2 since the strains were similar at the different temperatures.

The activation energies for secondary creep at 750°C and 850°C were similar: 527 kJmol<sup>-1</sup> and 505 kJmol<sup>-1</sup> respectively. Estimates of the activation energy for primary creep were 546 kJmol<sup>-1</sup> at 550 MPa, dropping to 296 kJmol<sup>-1</sup> and 230 kJmol<sup>-1</sup>, at 650 MPa and 750 MPa respectively. The activation energy for secondary creep is

Table 2: Activation energies  $E_a$ , for primary and secondary creep in CMSX-4; all primary results from two separate tests of the same orientation and the secondary from

stepped temperature tests.

Creep	Stress (MPa)	Temp Range°C	E <sub>a</sub> kJmol <sup>-1</sup>
Secondary	750	710-750	527
Secondary	550	790-850	505
Primary	750	750-850	230
Primary	650	750-850	296
Primary	550	750-850	546

Table 3. Stress exponents n from multiple tests (same orientation)

Alloy	Temp°C	Stress MPa	Creep	n
CMSX-4	750	450-750	Prim	20.3
CMSX-4	750	600-750	Sec	13.1
CMSX-4	850	550-750	Prim	14.0
CMSX-4	850	550-750	Sec	13.3
TMS75	750	550-750	Sec	11.0
TMS82	750	650-750	Sec	11.0
CMSX-	750	650-750	Sec	9.4
10				

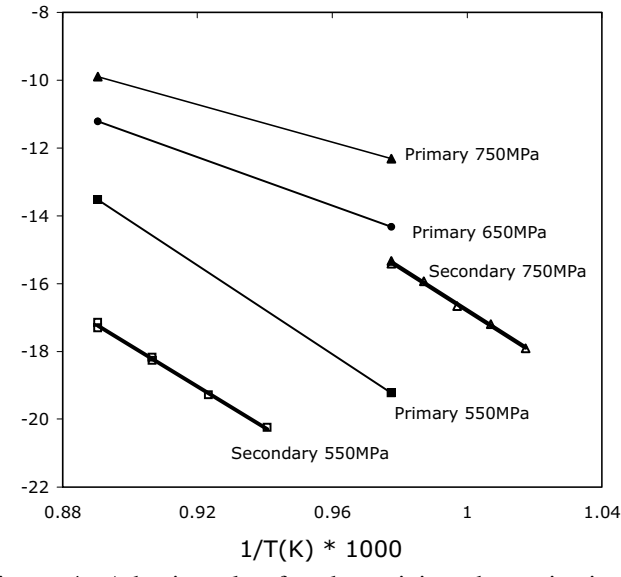


Figure 4; Arhenius plot for determining the activation energies of primary and secondary creep of CMSX-4.

almost double that for primary creep at higher stress, but this difference disappears as the stress falls to 550MPa. At this stress the primary creep strain has fallen below 1%.

In addition we have looked at the early stages of creep deformation in a number of alloys at various stresses at 750°C. Figure 3 shows the stress-strain curves for the alloys TMS75, TMS82, CMSX-10 and CMSX-4 at 750MPa and 650MPa. By using samples of the same orientation, the stress dependence of the minimum and maximum creep rates for CMSX-4 at 750°C and 850°C,

and for several alloys at  $750^{\circ}$ C, have been assessed. The results are presented in the log/log plot of strain rate against the real stress, Figure 5. The gradients give the exponential stress exponents, n Table 3. For all the alloys during secondary creeps at both temperatures, n lies within the range 9-13, but distinctively, at  $750^{\circ}$ C CMSX-4 a much higher exponent for the stress dependence of primary creep of 20 is observed. Following the activation energy determination described above, the same samples were used to assess the stress dependence by measuring the effect of a stress drop on the secondary creep rate. This gave a value of 10 for CMSX-4 during secondary creep at  $850^{\circ}$ C and 13 at  $750^{\circ}$ C.

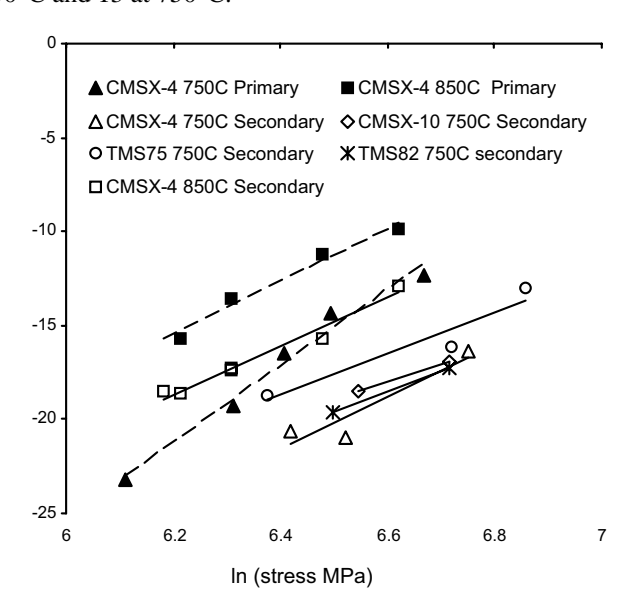


Figure 5, Graph showing the stress dependence of the primary and secondary creep rates for CMSX-4 at 750°C and 850°C and for various alloys at 750°C.

### Two stage creep tests:

Figure 6 shows stress strain plots of two creep tests from identically oriented specimens. One was tested at 750°C under 750MPa to failure; the second is a two-stage test, crept to 0.4% strain at 950°C and 485MPa, followed by testing to failure at 750°C and 750MPa. The pre-strain reduces the amount of primary creep in this orientation from 4.5% to 2% and in others by at least a half [13]. It also changes the fracture mode from a single macroscopic facetted failure following the {111} primary slip plane to a more irregular fracture surface where the fracture nucleates at multiple pores propagating as facetted failures on a local scale. The secondary creep portion of the single temperature test can over-lays the two-stage test when displaced by 3% strain and 200 hours. The two-stage test undergoes a further 4% strain prior to failure.

The effect of the pre-strain is to reduce the primary creep to 1/3, the maximum primary creep rate to 1/20, and to cause an incubation period of very low strain. At 20 hours this is

much longer than the original incubation period of 2 hours at the commencement of the single stage test.

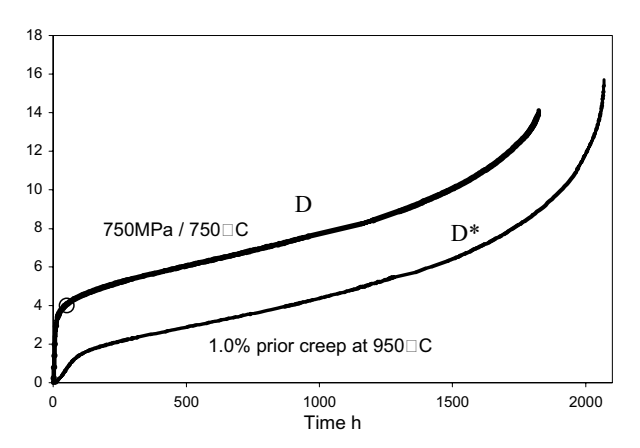
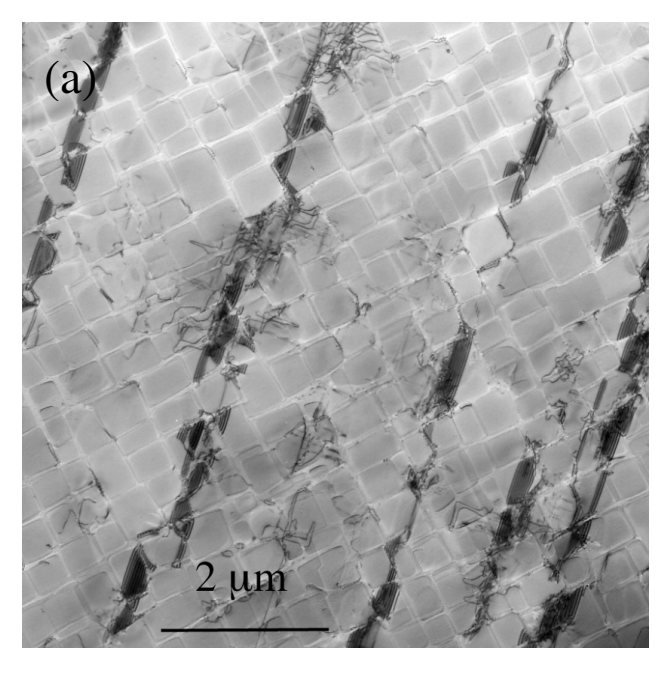


Figure 6. Creep curves from two stage tests D and D\* showing the decrease in primary creep rate and strain, but that secondary creep is virtually unaffected. The arrow shows where the creep rate equals the maximum value in D\*.

Figure 7 shows micrographs of the dislocation structure of two similar samples, I and I\*, with and without pre-strain, interrupted early in primary creep at  $750^{\circ}\text{C}/750\text{MPa}$ . At interruption the deformation rate in I was approximately 10 times that in I\*. Both contain stacking faults: in the case of the pre-strained sample these are in short segments stretching over two  $\gamma'$  precipitates at most. The density of dislocations at the  $\gamma/\gamma'$  interface was considerably higher in the two stage test I\*, consistent with the damage introduced at  $950^{\circ}\text{C}$ .

# Microstructural observations

The deformation microstructure of the specimen of orientation A, interrupted at the very start of secondary creep at 750°C and 750MPa, is shown in Figure 8. As expected, due to its orientation, there is extensive deformation by stacking faults but it is almost entirely on the primary slip system. There is no evidence that the transition to secondary creep is associated, in this orientation, with the extensive operation of slip on a secondary system. Stacking faults extend across one or two gamma prime precipitates and the gamma channels are well populated with dislocations accumulating at the  $\gamma/\gamma'$ This suggests that the prime hardening mechanism is not interaction between the primary system and a secondary system activated as the rotation of the sample approaches the duplex slip boundary, but the interaction with a/2<110> dislocations propagating through the y phase. In contrast an orientation much closer to the [001] pole but interrupted in the early stages of primary creep whilst the creep rate is still increasing, shows a lower density of dislocations, but the operation of three  $\{111\langle 11\overline{2}\rangle \text{ slip systems } [12].$ 



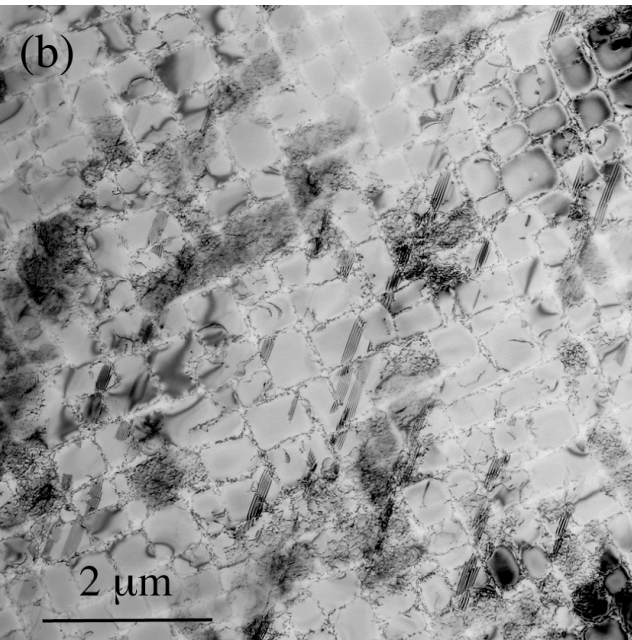


Figure 7: TEM micrographs of creep tests interrupted after 1% creep at 750°C (a), and similarly but following a prestrain at 950°C, (b).

The eccentricity of the test-pieces of orientation A was measured following deformation to the start of secondary creep (shown in Figure 8). Figure 9 shows a polar plot of  $r-r_o$ , where r is the local specimen radius and  $r_o$  is a constant for the two plots. Thus the deviation of the plot from the outer circle is proportional to the contraction of the sample. For the sample deformed to the end of primary creep (a), the contraction in the direction [110] is consistent

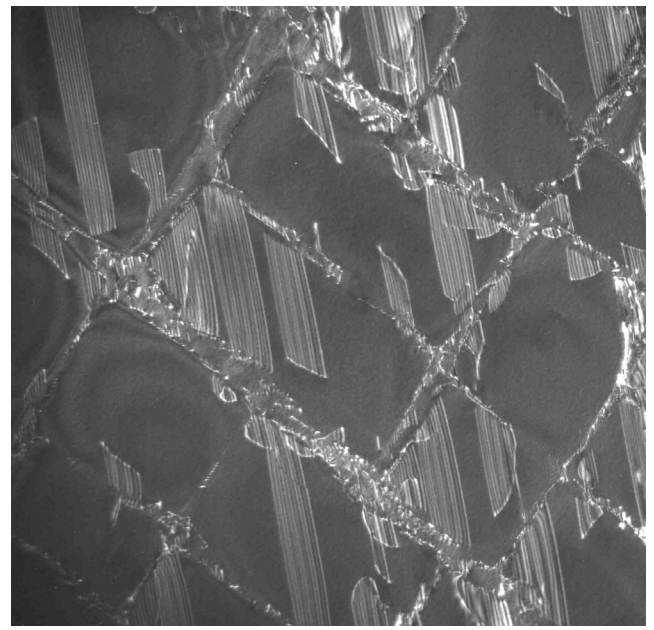
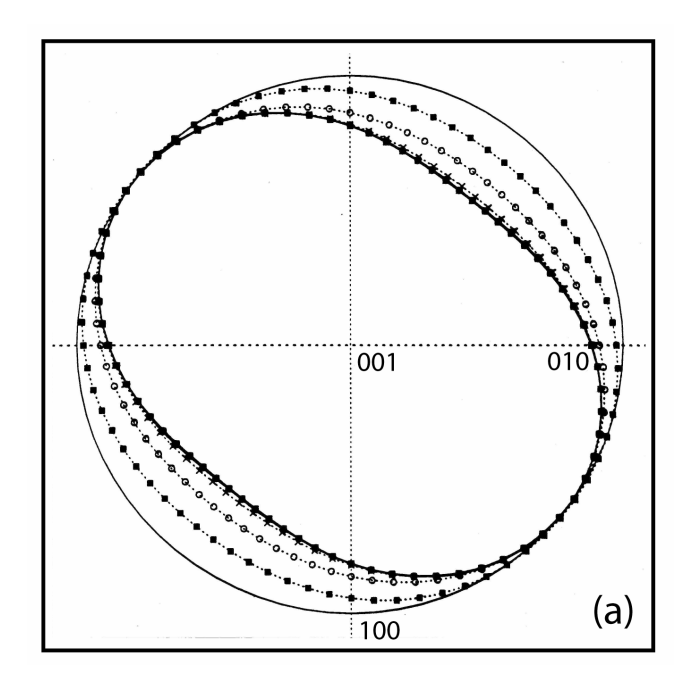


Figure 8. Weak beam micrograph of A deformed to the start of secondary creep at 750°C and 750MPa.

with slip on the system (111)[112] as expected. Slip continues on the\_same system throughout secondary creep to failure (b), demonstrating that the dominant slip system in primary creep is maintained through secondary creep. There is clearly also contraction in the orthogonal directions once secondary creep commences, thereafter the ratio of contraction on the primary system to that on the secondary (at right angles) is some 3:1.

## Effect of Alloy Composition

The quantity of primary creep strain varies greatly from alloy to alloy, Figure 4. The alloy TMS75 shows high primary creep strain, contrasting with the alloy TMS82. Further tests have confirmed that these trends are retained over a range of orientations. The alloys CMSX-4 and CMSX-10 lie between these two extremes with CMSX-10 retaining higher primary creep at low stress. Figure 11 shows the primary slip planes of the alloys TMS75 and TMS 82 after 1.4% strain. A difference in the structure of the stacking fault ribbons in these two alloys is observed: stacking faults separating the dislocations in TMS75 readily bridge the gap between the  $\gamma'$  precipitates resulting in extended stacking faults, whereas in TMS82 stacking faults are constrained within the  $\gamma'$  precipitates. The stress dependence of secondary creep rates for all alloys are broadly similar for the various alloys at 750°C and the power exponent n varies between 10 and 13.



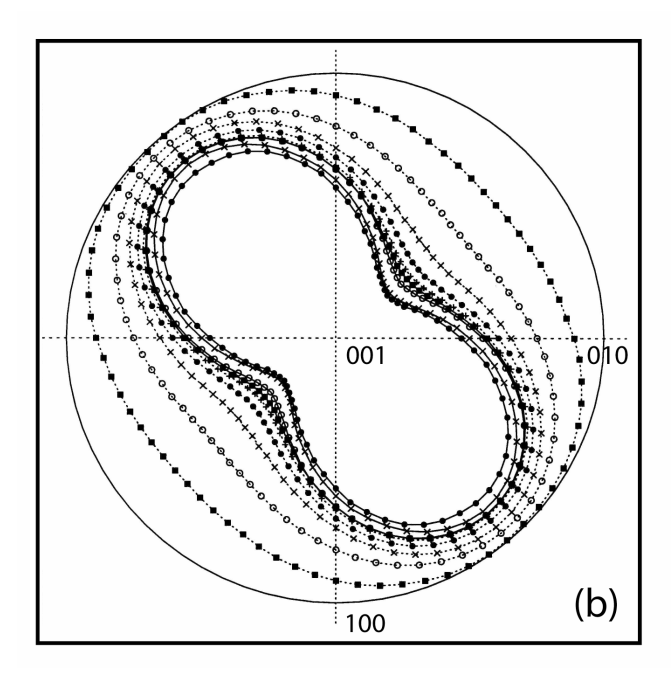
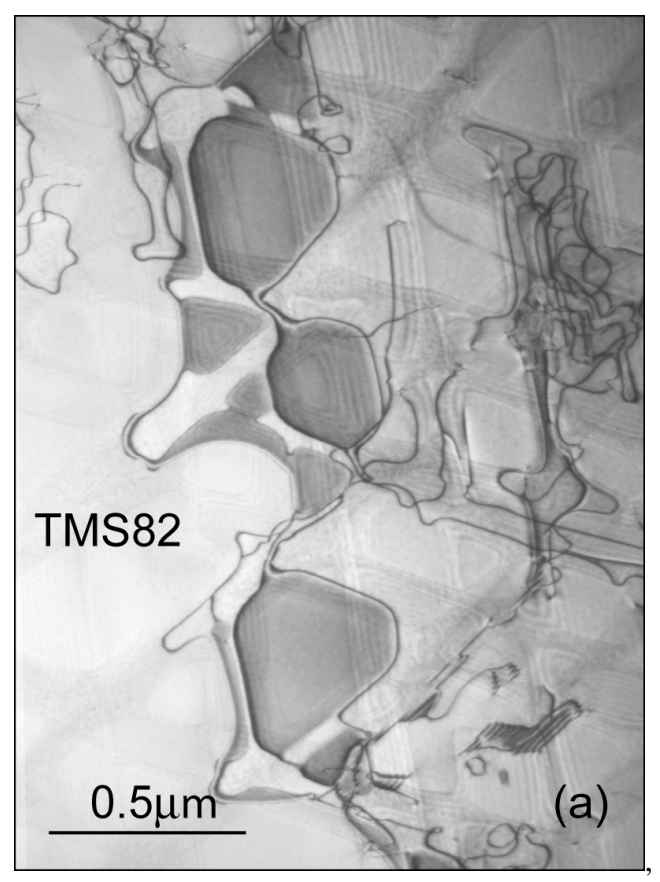


Figure 9: Polar plot of  $r - r_0$  relative to the approximate [010] and [100] sample directions showing the contraction in the radius of specimen orientation A, following creep to the end of primary creep (a) and to failure (b).



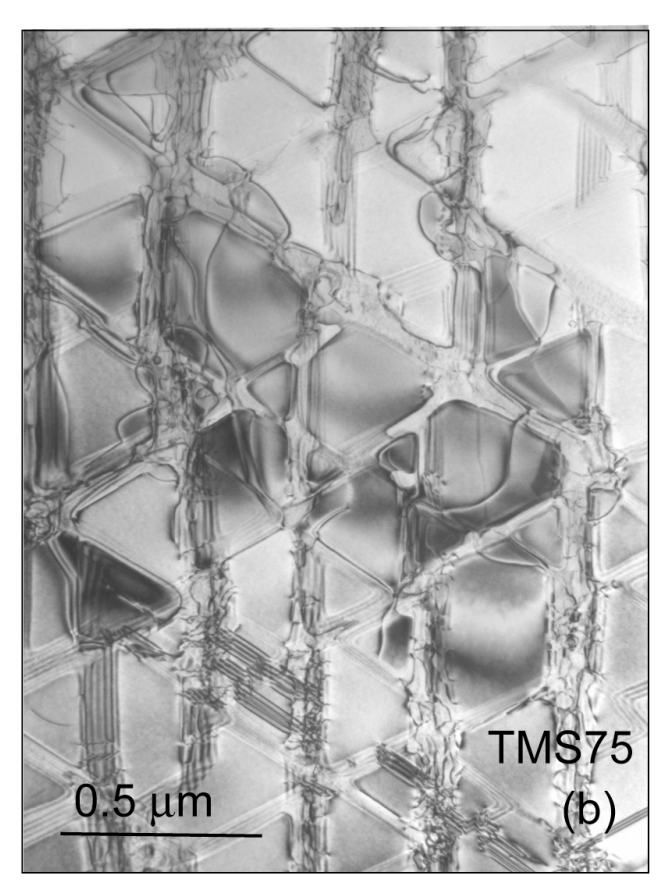


Figure 10. Stacking fault ribbons on the primary slip plane in the alloys TMS82 and TMS75 interrupted at 1.4% strain at 750°C and 750MPa, showing how the stacking faults are able to extend across the  $\gamma$  channels in TMS75 and hence move more easily through the  $\gamma/\gamma$  microstructure leading to more rapid primary creep.

#### Discussion

The range of temperature and stress (750°C - 850°C and ≥ 550MPa) where the major mechanism of deformation is  $\{111\sqrt{112}\}$  dislocation ribbons passing through both  $\gamma$ and  $\gamma'$  phases, coincides with the distinctive low values for the activation energy and high stress dependence. Thus creep deformation by stacking fault shear in this temperature range and at high stresses is distinct from creep at lower stresses and/or higher temperatures consistent with the observations in [4]. All alloys interrupted during primary creep show the presence of dislocation ribbons consisting of intrinsic and extrinsic faults. These ribbons show distinctive morphologies in each alloy: widely separated and convoluted for the alloy TMS75 showing the most primary creep, compact and restricted in the alloy TMS82 showing consistently the smallest amount of primary creep. Thus for the same density of mobile <112> dislocations a section cut on (001) of these two alloys would show very different densities of stacking fault purely as a result of the width of the dislocations and not the density of active dislocation ribbons.

The spread of the dislocation ribbons over several  $\gamma'$ precipitates can occur when the stacking fault energy in the  $\gamma$  phase is low enough for the superlattice intrinsic and extrinsic faults to extend across the y as an 'ordinary' FCC stacking fault with no dislocation at the  $\gamma/\gamma'$ interface. Thus in TMS75 the a/3<112> dislocations making up the ribbon appear able to pass through both phases without a change in structure. The change from SISF or SESF to APB at every  $\gamma/\gamma'$  interface, as is necessary in TMS82, represents a barrier to rapid movement of the ribbon. The higher mobility of the ribbon results in the higher primary creep levels at all orientations in TMS 75. It seems plausible that the high cobalt content of the alloy TMS75 (12 wt%) lowers the stacking fault energy in the  $\gamma$  phase and thus promotes stacking fault shear. This property is consistent with the observations of Murakami et. al. [10] that creep in cobalt containing alloys is highly sensitive to orientation. Other HCP elements such as rhenium may also lower stacking fault energy and promote high primary creep strains [8].

At orientations where the Schmid factors are equally balanced between active systems [12,16] stacking fault shear occurs on several {111} planes throughout primary

creep. In contrast, examination of the microstructures of a test A, oriented for high primary creep on predominantly one  $\{111\sqrt{112}\}$  system and interrupted at 8% strain at the beginning of secondary creep (Figure 8), shows little evidence that the interaction of the primary system with a conjugate system to produce the hardening necessary for the transition to secondary creep. The density of secondary systems is very low even though the creep rate has dropped to 5% of the maximum value. However, the presence of multiple  $\{111\}\langle11\overline{2}\rangle$  systems throughout primary creep decreases the primary creep rate as the systems intersect. For example, orientation A has a maximum creep rate more than three times that of D which has two systems with very similar Schmid factors (0.480 and 0.486) whereas those of A are 0.496 and 0.478. A stress exponent of 10 would predict an increase in strain rate of 22% from the difference in Schmid factor alone.

At the end of primary creep in orientation A the density of dislocations in the  $\gamma$  channels is high, with most channels populated. This suggests strongly that it is the penetration of the gamma channels by dislocations that is the principal cause of the transition to secondary creep. This is confirmed by the effect of introducing a network of dislocations into the y in the two stage creep tests. The maximum primary creep rate is reduced by a factor of 21 times - this corresponds to the rate occurring in the single-stage test on the cusp between primary and secondary creep at a strain of 4% (indicated on graph, Fig. Nevertheless, prior damage at 950°C does not eliminate primary creep: clearly there are differences in the dislocation structure formed at 950°C and that during secondary creep at 750°C. There is thus a period of accelerated creep at the start of the two-stage test as the structures converge, but quite rapidly the progress of creep becomes identical in the two tests provided the strain is low enough for the reduction in area not to be an issue. The effect of the pre-strain persists, however, in the mode of fracture.

It is not surprising that prior deformation causes hardening as observed in the two-stage tests, but it is significant that that the introduction of the dislocation network in the  $\gamma$  phase has the effect of reducing the creep rate to a level typical of the transition range from primary creep, and that the subsequent secondary creep appears to follow precisely the same path as the single stage test. It is also significant that stacking faults continue to be generated following the establishment of a network of dislocations in the  $\gamma$ . The origin of the 20-hour incubation period is the subject of further work and may have its origin in the decrease in misfit during the temperature drop from 950°C to 750°C and the consequent back-stress that this creates.

Having produced the dislocation structure necessary for steady state creep, we examine the mechanism by which secondary creep occurs. The evidence from the rotation of the tensile axis as a function of the strain [12] and the eccentricity of the deformed sample, Figure 9, shows that there is no discontinuity in the deformation geometry at the transition from primary creep and that the rotation continues to be consistent with the operation of  $\{111\/ 11\overline{2}\}$ shear. The radius reduction during the primary creep is exclusively in the direction of the primary Burgers vector and remains three times that in the secondary systems during secondary creep. This, together with the microstructural evidence of the continued generation of stacking faults where conditions are favourable, suggests strongly that the principal deformation mechanism in secondary creep is the shearing of the γ' by partial dislocations trailing stacking faults.

Much work has been published identifying the mechanisms by which of stacking faults form from combinations of dislocations in the  $\gamma$  [16,17,18]. For example, one commonly observed reaction (although by no means the only one) is of the type:

$$a/2[101] + a/2[011] \rightarrow a/6[112] + SISF + a/3[112]$$

We have shown that the stacking faults observed in secondary creep are not debris from primary creep, but are continually generated and participate in the deformation process. However, the high density of dislocations at the  $\gamma/\gamma'$  interface, and particularly in the horizontal channels where for negative misfit the density is highest, means that these dislocations are able only to cross one or two precipitates before intersecting dislocations at the precipitate perimeters. Deformation requires further dislocation interactions at the  $\gamma/\gamma'$  interface.

The dislocations observed in the  $\gamma'$  will continue to reflect those available in the  $\gamma'\gamma'$  interface and the orientation of the tensile axis. Defects will be present in proportion to the resolved shear stress, and the nucleation of stacking faults where the range of Burgers vectors in the  $\gamma$  is restricted remains an issue in secondary creep [12]. The close association observed between primary creep strain and the secondary creep rate [4] follows, since the same conditions of high Schmid factor and ease of nucleation which favour high primary creep, will also increase the density of superlattice partial dislocations crossing the  $\gamma'$  phase and hence the creep rate during steady state creep.

The observed change in activation energy on entering secondary creep suggests that it is the combination, by climb, of dislocations to produce mobile faults, and not the transmission of the fault through the  $\gamma'$ , which is the slowest, rate-determining, process. Thus climb in the  $\gamma/\gamma'$ 

interface is associated with the higher activation energies of ~530kJ mol<sup>-1</sup>. This is closer to the values measured for high temperature creep at (627kJmol<sup>-1</sup>) [4] and at the lower stresses of 550MPa, (550 kJmol<sup>-1</sup>) where stacking faults are not the principal shear mechanism.

In primary creep, where the motion of the dislocation ribbons, once nucleated, is relatively unimpeded, a ribbon can shear several hundred precipitates and the appropriate activation energy will be that associated with the movement of the ribbon, this appears to be the much lower value of ~230kJmol<sup>-1</sup>. As this involves repeated change in the dislocation structure but no climb, the diffusive process could be via the dislocation ribbon itself.

### **Conclusions:**

- Primary creep at 750°C and high stress has a
  distinctive mechanism characterised by a low
  activation energy and a high stress dependence. The
  activation energy rises at low stress and for secondary
  creep, to a value comparable with that at higher
  temperatures.
- Several systems are active from the beginning of primary creep especially where the Schmid factors are similar.
- The orientation dependence of primary creep is determined by a combination of the ease of nucleation, propagation and hardening: Primary creep disappears when nucleation of dislocations is not possible or the resolved shear stress is below a certain threshold.
- 4. Primary creep can be consistently reduced but not eliminated by introducing dislocations into the  $\gamma$ . Thus primary creep appears to be largely terminated by the propagation of dislocations in the  $\gamma$ , but the creep rate is reduced by the activation of, and interaction with, a second stacking fault shear system.
- 5. During secondary creep a large proportion of the strain occurs by the movement of dislocations through the  $\gamma'$ , but the activation energies suggest that the formation of dislocation configurations able to enter the  $\gamma'$  is the rate determining process during secondary creep, and not the rate at which they move through the  $\gamma'$ .

# Acknowledgments

The authors would like to thank Rolls-Royce plc and DSTL for their financial support of this work and the provision of materials. In particular we would like to

acknowledge the contribution of Bob Broomfield to all aspects of this work. Thanks are also due to Prof. H. Harada of NIMS, Japan, for the provision of materials and H. Tamaki of Hitachi Ltd for performing some of the creep tests. GLD would like to acknowledge the support of the Cambridge Commonwealth Trust.

## References

- D.W. MacLachen and D.M. Knowles, Fatigue Fracture Engineering Materials Struct 25, (2002), 399-409.
- 2. R.A. MacKay and R.D. Meier, Metall. Trans., 13A, (1982), 1747-1754.
- 3. P. Caron, Y. Ohta, Y.G. Nakagawa and T. Kahn, Superalloys 1988, eds. S. Reichman, D.N. Duhl, G. Maurer, S. Antolovich and C. Lund, the Metallurgical Society of AIME, PA USA, (1988), 215-224.
- N. Matan, D.C. Cox, P. Carter, M.A. Rist, C.M.F. Rae, R.C. Reed, Acta Mater., 47, (1999), 1549-1563.
- 5. G.R. Leverant and B.H. Kear, Metall. Trans., 1, (1970), 491.
- 6. K. Kakehi, Mat. Sci. Eng., A278, (2000) 135–141.
- 7. A. Hopgood and J.W. Martin, Mat. Sci. and Eng., 82, (1986), 27-36.
- 8. C.M.F. Rae, K. Kahehi and R.C. Reed, Proceedings of the 7<sup>th</sup> Liege Conference on 'Materials for Advanced Power Engineering' Eds J. Lecomte-Beckers, M. Carton, F. Schubert and PJ Ennis, p207.
- 9. C.M.F Rae, T. Smeeton, M.A. Rist and R.C. Reed, Mat Science and Engineering, in press.
- 10. H. Murakami, T. Yamagata, H. Harada and M. Yamazaki, Mat. Sci. Eng., A223, (1997) 54-58.
- 11. C.M.F. Rae, N. Matan and R.C. Reed, and Materials Science Engineering, A300, (2001) 125-134.
- 12. C.M.F. Rae, N.Matan, D.C. Cox, M.A. Rist and R.C. Reed, Metall. Trans., 31A, (2000), 2219-2227.
- G.L.Drew, PhD Thesis, University of Cambridge 2004.
- 14. G.R.Leverant, B.H. Kear and J.M. Oblak, Metall. Trans. Vol.4, (1973), 355-362.
- V. Sass, U. Glatzel and M. Feller-Kniepmeier, Superalloys 1996, Eds R.D. Kissinger et al, The Minerals Metals and Materials Society, (1996) pp 283-290.
- 16. Q.Z. Chen and D.M. Knowles, Materials Science and Engineering, A356, (2003) 352-367.
- 17. R. Bonnet and A. Ati, Acta Metall. 8, (1989), 2153-
- 18. M. Condat and B. Decamps, Scripta Met, Vol. 21, (1987), 607-612.